



The electrochemical and local structural analysis of the mesoporous $\text{Li}_4\text{Ti}_5\text{O}_{12}$ anode



Soojeong Kim ^a, Shaohua Fang ^b, Zhengxi Zhang ^b, Jizhang Chen ^b, Li Yang ^b,
James E. Penner-Hahn ^a, Aniruddha Deb ^{a,*}

^a Department of Chemistry, University of Michigan, Ann Arbor, MI 48109, USA

^b School of Chemistry and Chemical Technology, Shanghai Jiao Tong University, Shanghai 200240, PR China

H I G H L I G H T S

- Hydrothermal synthesis of titanate microspheres with large surface area/thin walls.
- Samples have improved voltage profiles and charge/discharge dynamics.
- Stable cycling performance, with 140 mAh g⁻¹ capacity retention after 4000 cycles.
- *In-situ* XANES shows conversion between Ti⁴⁺ and Ti³⁺ during charge/discharge cycling.
- *In-situ* EXAFS reveals small changes $R_{\text{Ti-O}}$ but no detectable change in $R_{\text{Ti-Ti}}$.

A R T I C L E I N F O

Article history:

Received 24 March 2014

Received in revised form

22 May 2014

Accepted 3 June 2014

Available online 11 June 2014

Keywords:

Lithium battery

Anodes

X-ray absorption spectroscopy

In-situ X-ray spectroscopy

A B S T R A C T

Mesoporous lithium titanate microsphere anodes have been made by hydrothermal synthesis. Layered hydrous lithium titanate was obtained after hydrothermal reaction and $\text{Li}_4\text{Ti}_5\text{O}_{12}$ microspheres assembled from nanosheets were subsequently formed by thermal treatment. This results in improved voltage profiles and charge/discharge dynamics. Mesoporous lithium titanate microspheres showed stable cycling performances, with high capacity retention (140 mAh g⁻¹) even after 4000 cycles. In order to understand the functioning of this promising anode material at the molecular level, we used *in-situ* X-ray absorption spectroscopy (XAS). The XAS results verify the Ti conversion between Ti⁴⁺ and Ti³⁺ during charge/discharge cycling and demonstrate that this reduction is accompanied by small changes Ti–O distance but no detectable change in Ti–Ti distance. This anion re-arrangement suggests a structural explanation for the fact that this material is electrochemically very stable even under higher current density cycling.

© 2014 Elsevier B.V. All rights reserved.

1. Introduction

Rechargeable Li-ion materials are widely used in hybrid electric vehicles, portable electronic devices, and advanced electrochemical energy storage devices due to their relatively high energy/power density, safety, and cycle life [1–4]. Nevertheless, there remain major impediments to their further adoption and for many industrial needs. Li-ion intercalation materials lack sufficient power density and cycle life. For robust automotive applications the choice of the electrode materials is determined by cost factors as well as the ability to deliver the necessary energy (and power) without undergoing material degradation/failure. In order to overcome

these limitations, efforts have been made to find new materials for both the cathode and the anode, to understand at the molecular level how these new classes of electrode materials function in electrochemical energy storage devices, and to use this knowledge to inform the design of new materials which will lead to the improvement of the total battery system [4,5].

One particular problem with Li-ion materials is the fact that lithiation and delithiation can cause significant volume changes which, in turn, can result in severe degradation of the electrodes, strongly limiting the life time of the battery. One promising candidate anode material is the mesoporous spinel $\text{Li}_4\text{Ti}_5\text{O}_{12}$. An advantage of $\text{Li}_4\text{Ti}_5\text{O}_{12}$ is its “zero-strain” property, in which the lithiated and delithiated phases show almost identical lattice parameters [6,7]. In contrast to graphite, where lithium intercalation leads to exfoliation and structural strain, lithium can freely

* Corresponding author.

E-mail address: debani@umich.edu (A. Deb).

intercalate into the crystal lattice of lithium titanate and deintercalate without significant structure deformation. A second advantage of $\text{Li}_4\text{Ti}_5\text{O}_{12}$ as an anode is its safety compared to conventional graphite anodes; long cycling of graphite electrodes can result in the formation of metallic lithium dendrites which can cause a short circuit. However, a major limitation of $\text{Li}_4\text{Ti}_5\text{O}_{12}$ as an anode material is the fact that bulk $\text{Li}_4\text{Ti}_5\text{O}_{12}$ has poor electronic conductivity which limits its capacity at high charge/discharge rates [8,9]. In an effort to overcome this limitation, various morphologies have been explored, including nanowires, nanotubes, nanorods, nanosheets and nanoparticles with the goal of maximizing effective surface area in order to minimize conductivity limitations and thus maximize the rate [10]. We have chosen to work with $\text{Li}_4\text{Ti}_5\text{O}_{12}$ in the form of hollow microspheres because nanostructures of this sort have been shown to have shortened diffusion distances and higher surface areas, thus promising higher charge/discharge rates [11–15]. But we should also mention here as a drawback the hollow structure leads to decrease in volumetric energy density. In comparison with graphite, mesoporous $\text{Li}_4\text{Ti}_5\text{O}_{12}$ microspheres present several attractive features including a flatter voltage profile, higher surface area, greater stability to repeated cycling, and good lithium-ion mobility.

Here, the hydrothermal synthesis technique [10,16] has been used to produce layered hydrous lithium titanate which was transformed by thermal treatment to $\text{Li}_4\text{Ti}_5\text{O}_{12}$ microspheres assembled from nanosheets. This hollow microsphere structure (shown in Fig. 1) is interesting due to its large surface area and thin walls, and its theoretically predicted (from earlier investigations) [17–19] that leads to decrease in the current density per unit surface area and shorten the Li-diffusion length in the solid phase, ultimately giving improved voltage profiles and charge/discharge dynamics. These promising points motivated us to investigate this material using *in-situ* X-ray absorption spectroscopy (XAS) in order to fully characterize its structural properties under real operating conditions.

XAS includes both X-ray absorption near edge structure (XANES) and extended X-ray absorption fine structure (EXAFS). XANES gives information about the oxidation state of the absorbing atom (in this sample Ti), and, through the 1s–3d transition, insight into the titanium electronic structure. This also helps us to understand the charge compensation mechanism of the system during cycling. The EXAFS provides direct information about the local structure of the titanium. By using *in-situ* measurements, we can learn about how the electronic and atomic structure change as a function of the state of charge (SOC) during cycling.

2. Experimental

2.1. Sample preparation and characterization

Typically, 1 mL H_2O_2 aqueous solution (30%) and 0.618 g titanium tetraisopropoxide (TTIP) were added to 20 mL of 0.5 M LiOH aqueous solution, followed by stirring at room temperature for 0.5 h. This suspension was transferred into a 30 mL autoclave, which was maintained at 130 °C for 20 h and then cooled to room temperature naturally. After centrifugation the white precipitate was washed with water, dried at 80 °C, and was then calcined in a muffle furnace at 500 °C for 2 h in air. X-ray powder diffraction (XRD) measurements were conducted by a Rigaku D/max-2200/PC diffractometer. The morphology was analyzed by field emitting scanning electron microscopy (FE-SEM, JEOL JSM-7401F) and transmission electron microscopy (TEM, JEOL JEM-2010).

2.2. Electrode preparation

Electrochemical tests were carried out using CR2016 coin-type half cells, assembled in an argon-filled glove box (M. Braun Co., $[\text{O}_2] < 1$ ppm, $[\text{H}_2\text{O}] < 1$ ppm). For preparing working electrodes, a mixture of $\text{Li}_4\text{Ti}_5\text{O}_{12}$, acetylene black, and polyvinylidene fluoride

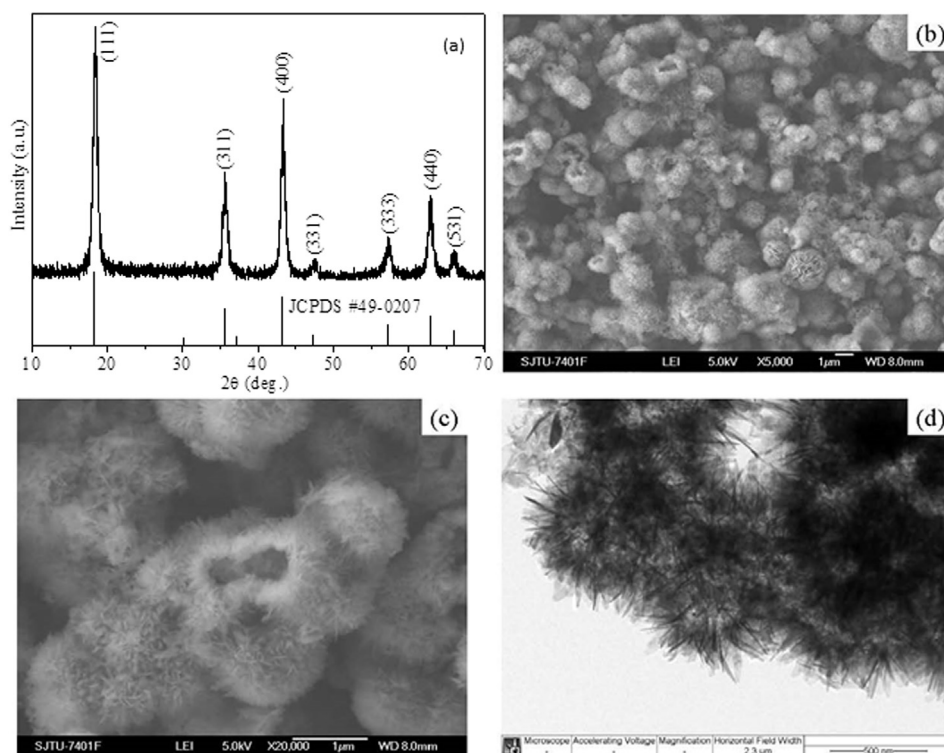


Fig. 1. (a) XRD pattern of $\text{Li}_4\text{Ti}_5\text{O}_{12}$, (b, c) SEM with different magnification and (d) TEM micrograph images.

(PVDF) binder at a weight ratio of 80:10:10 was pasted on pure copper foil. Pure lithium foil was used as the counter electrode, and glass fiber (GF/A) from Whatman was used as the separator. The separator was soaked with an electrolyte consisting of 1 M LiPF_6 dissolved in 50 wt % ethylene carbonate (EC) and 50 wt % dimethylcarbonate (DMC) obtained as a solution from BASF Company. The assembled cells were cycled under different current densities (shown in Fig. 2) within the voltage range of 2.5–1.0 V using a CT2001A cell test instrument (LAND Electronic Co.) at room temperature.

2.3. In-situ XAS experiments

Electrochemical XAS cell assembly was done in an argon-filled glove box. The separator was punched to give a disk with an outer diameter of 20 mm. The separator was placed on top of the electrode $\text{Li}_4\text{Ti}_5\text{O}_{12}$ soaked in 1 M LiPF_6 electrolyte, dissolved in 50 wt % ethylene carbonate (EC) and 50 wt % dimethylcarbonate (DMC) obtained as a solution from BASF. Finally, a lithium foil, counter-electrode was punched to give a disk with an outer diameter of 14 mm and an inner diameter of 8 mm and placed on top of the separator which was soaked with electrolyte. Kapton film (25.4 μm thickness) was utilized as the X-ray window for this *in-situ* electrochemical reaction cell. More detailed information on the design of this reaction cell can be found in Deb et al. [20].

For the XAS measurements, electrochemistry was performed using a Princeton Applied Research VERSASTAT potentiostat to cycle the electrochemical reaction cell. XAS measurements were performed while the electrochemical cell was cycled at a current density of 175 mA g^{-1} (1 C) between 1.0 and 2.5 V (vs. Li/Li^+)

(Fig. S4). Two model compounds, Ti_2O_3 (Ti^{3+}) and TiO_2 (Ti^{4+}), were measured as XANES references.

In-situ XAS measurements were performed as previously described [21]. Spectra were measured in transmission mode at the DND-CAT sector 5, at the Advanced Photon Source, using a water cooled $\text{Si}(111)$ double crystal monochromator and a beam size of $0.3 \times 4 \text{ mm}^2$ so that the beam could pass completely through the *in-situ* cell X-ray window. The incident photon flux was $\sim 10^{10}$ photons s^{-1} X-ray flux before and after the electrode sample were measured using N_2 filled ion chambers. A Ti foil reference and a third ion chamber were placed behind the sample in order to provide an internal energy reference with the first inflection point of the Ti-foil defined as 4966 eV. For the Ti K absorption edge the monochromator was scanned from 200 eV below to 800 eV above the edge. Scans (using 5 eV steps in the pre-edge region, 0.5 eV steps in the near-edge region and 0.05 \AA^{-1} steps in the EXAFS region) were taken at each applied voltage for analysis. The data were integrated for 1 s per step in the pre-edge, 1.5 s per step in the near edge region and 1.5–25 s per step in the EXAFS region for a total scan time of about 40 min. Two scans were made at each potential and averaged.

The XANES data shown here were analyzed using the MBACK program, [22] and the EXAFS data were analyzed using the IFEFFIT [23] software package. A pre-edge background and a cubic spline EXAFS background were subtracted and the EXAFS oscillations were normalized to the appropriate Victoreen function modeling the absorption decrease above the edge [24]. An E_0 value of 4987.2 eV was used to calculate k . The EXAFS, $\chi(k)$, was weighted by k^2 in order to correct for the damping at high k . Fourier transforms were calculated as $k^2\chi(k)$ over a k range of 1.0–10.5 \AA^{-1} . The EXAFS fitting was done by IFEFFIT package using FEFF9 [25] to calculate *ab initio* phase and amplitude parameters.

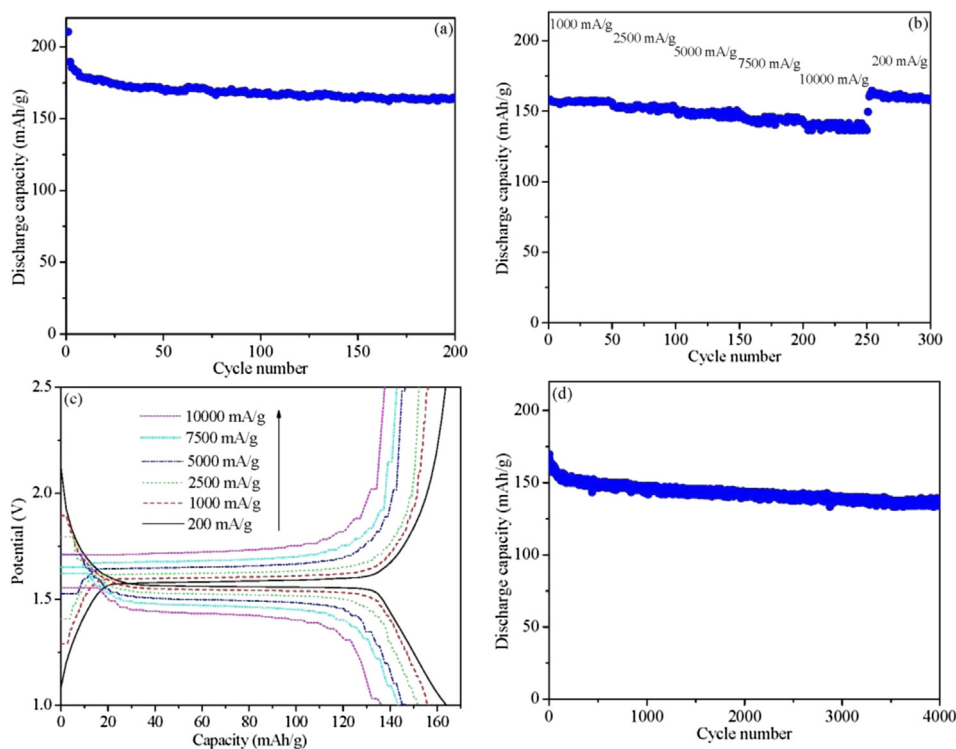


Fig. 2. (a) Cycling performance at 200 mA g^{-1} ; (b) rate performance of $\text{Li}_4\text{Ti}_5\text{O}_{12}$ from 200 mA g^{-1} to $10,000 \text{ mA g}^{-1}$ (1.1 C, 5.7 C, 14.3 C, 28.6 C, 42.9 C, 57.1 C), the electrode loading was -0.65 mg cm^{-2} ; (c) galvanostatic discharge/charge curves at different current densities. The average discharge capacities at each current density are 156.7 mAh g^{-1} at 1000 mA g^{-1} , 152.5 mAh g^{-1} at 2500 mA g^{-1} , 148.2 mAh g^{-1} at 5000 mA g^{-1} , 144.0 mAh g^{-1} at 7500 mA g^{-1} , and 139.1 mAh g^{-1} at $10,000 \text{ mA g}^{-1}$; (d) long-term cycling performance at 2500 mA g^{-1} of $\text{Li}_4\text{Ti}_5\text{O}_{12}$.

3. Results and discussion

3.1. Material characterization

The XRD pattern for the material is shown in Fig. 1a. Seven peaks at ca. 18.3°, 35.5°, 43.3°, 47.3°, 57.2°, 63.0° and 66.1° are ascribed to the (111), (311), (400), (331), (333), (440), and (531) reflections of spinel $\text{Li}_4\text{Ti}_5\text{O}_{12}$ (Fd3m, space group no. 227) and the XRD pattern of our sample can be indexed to spinel $\text{Li}_4\text{Ti}_5\text{O}_{12}$ standard in the Joint Committee on Powder Diffraction Standards (JCPDS) database (JCPDS #: 49-0207). No impurities were detected. The broad peaks in the XRD suggest that the $\text{Li}_4\text{Ti}_5\text{O}_{12}$ has a small crystallite size where the mean crystallite size of our sample is calculated to be ca. 12.1 nm using the Scherrer equation.

3.2. Electron microscopy

The microstructures of the samples were investigated mainly by TEM and SEM images. Representative electron microscope images of the material are shown in Fig. 1b–d. Fig. 1b shows the panoramic SEM image of the as prepared sample, which is composed of monodispersed microspheres (with diameters ranging from 400 to 600 nm) with a rough surface. Fig. 1c shows that the microspheres have a hollow structure and appear to have been formed from nanosheets. The magnified TEM micrograph (Fig. 1d) shows that the microspheres typically have a mean diameter of several hundred nanometers. From the TEM it is clear that the microspheres have spikes on their surface. These morphological features should increase the amount of active material that is in contact with the electrolyte, and are thus expected to enhance the electrochemical behavior of this material.

3.3. Surface area determination

In order to determine the total pore volume, we measured N_2 adsorption/desorption isotherms, and confirmed by Barrett–Joyner–Halenda (BJH) analysis the total pore volume of our samples was $0.255 \text{ cm}^3 \text{ g}^{-1}$, while the Brunauer–Emmett–Teller (BET) isotherm analysis was performed to obtain the specific surface area which was $68.9 \text{ m}^2 \text{ g}^{-1}$ (shown in Fig. S3, Supplementary material; the estimated uncertainty for both surface area and pore volume is $\sim \pm 1\%$). The specific surface area was larger for this hydrothermally prepared mesoporous samples than for samples prepared using other methods [26–29]. This suggests that the mesoporus hydrothermally prepared hollow microsphere sample should have better contact with the electrolyte and hence better electrochemical performance.

3.4. Electrochemical characterization

Electrochemical performance of $\text{Li}_4\text{Ti}_5\text{O}_{12}$ (theoretical capacity of 175 mAh g^{-1}) was first investigated by galvanostatic test measurements at 200 mA g^{-1} between 2.5 and 1.0 V (see Fig. 2a). The initial discharge capacity of 211 mAh g^{-1} declines to 190 mAh g^{-1} on the second cycle with a further decline to $\sim 164 \text{ mAh g}^{-1}$ over the next 200 cycles (a loss rate of $\sim 0.13 \text{ mAh g}^{-1}$ per cycle). One possible cause of this $\sim 22\%$ irreversible capacity loss is irreversible lithium storage into the surface, interface and interior of $\text{Li}_4\text{Ti}_5\text{O}_{12}$. After 200 cycles at 200 mA g^{-1} , the cycling stability of $\text{Li}_4\text{Ti}_5\text{O}_{12}$ was investigated at rates from 10^3 to 10^4 mA g^{-1} with 50 cycles at each current density (Fig. 2b). The average discharge capacities of $\text{Li}_4\text{Ti}_5\text{O}_{12}$ at each current density were only weakly dependent on current density, ranging from 156.7 mAh g^{-1} at 10^3 mA g^{-1} to 139.1 mAh g^{-1} at 10^4 mA g^{-1} . When the current density returned to

200 mA g^{-1} , the capacity of $\text{Li}_4\text{Ti}_5\text{O}_{12}$ recovered to 160.0 mAh g^{-1} (Fig. 2b).

As the current density was increased from 200 to 10^4 mA g^{-1} step wise, the spacing between discharge and charge plateaus increased Fig. 2c. This is most likely caused by electrochemical polarization at high current due to limitations in the transport speed of Li^+ . Previously it has been observed that increased polarization is associated with increased spacing between the plateaus when the current density is low, while in the case of the high current density and severe polarization, the plateaus disappear [30]. Hence, our observation that even at a very high current density of 10^4 A g^{-1} , the plateau is well preserved, suggests that there is relatively low polarization in $\text{Li}_4\text{Ti}_5\text{O}_{12}$. We think the steps in the charge/discharge cycles shown in Fig. 2c, especially at high current arises from the large deviation from equilibrium at high current densities. This excellent electrochemical performance is attributed to the architecture of hollow microspheres assembled from nanosheets [10,16].

These data indicate that the sample can endure wide changes at different current densities to retain an exceptional stability upon cycling. This performance is much better than that has been reported previously for $\text{Li}_4\text{Ti}_5\text{O}_{12}$. For example, Chou et al. [31] and Gao et al. [32] have both reported $\text{Li}_4\text{Ti}_5\text{O}_{12}$ having similar capacity at low rate; however, both found much worse capacity fall-off at high rate ($\sim 75 \text{ mAh g}^{-1}$ at 40 C for Chou et al. [31] vs. our observations of $\sim 140 \text{ mAh g}^{-1}$ at 57 C and $\sim 120 \text{ mAh g}^{-1}$ at 5 C for Gao et al. [32] vs. our observation of $\sim 156 \text{ mAh g}^{-1}$ at 5.7 C). Also, Chou et al. [31] used a higher mass loading for $\text{Li}_4\text{Ti}_5\text{O}_{12}$ electrode, $\sim 4 \text{ mg cm}^{-2}$, compared to our low mass loading of $\sim 0.65 \text{ mg cm}^{-2}$, which might be another reason for better rate performance (as was shown earlier by Bein et al. [33]). Liu et al. [34] have investigated self-supported $\text{Li}_4\text{Ti}_5\text{O}_{12}$ -C nanotube arrays and found similar (although somewhat lower) capacity then we see. However, their cycling stability ($\sim 7\%$ capacity loss after 500 cycles at a rate of 10 C) is noticeably worse than our stability ($\sim 17\%$ loss after 4000 cycles, Fig. 2d) at a slightly higher rate (14.3 C vs. 10 C) (more comparison can be found in Table S5, Supplementary information).

3.5. XANES of charge/discharge

The XANES spectrum for as-prepared $\text{Li}_4\text{Ti}_5\text{O}_{12}$ is compared with those for authentic Ti(III) and Ti(IV) models in Fig. 3a. Although the detailed structure of the XANES spectrum of $\text{Li}_4\text{Ti}_5\text{O}_{12}$ is different from that of either model, the edge energy is essentially the same as that of TiO_2 model compound, suggesting that the oxidation state of Ti in the as prepared material is primarily tetravalent Ti^{4+} . XANES spectra for the $\text{Li}_4\text{Ti}_5\text{O}_{12}$ anode during discharge and charge are shown in Fig. 3b and c, respectively. The edge shifts to lower energy on discharge and returns to higher energy during the charge cycle. To a first approximation, the edge shape is unchanged during electrochemical cycling, indicating that there is no significant change in the Ti environment. A variety of different points might be used to define the edge energy. These are labeled on Fig. 3b: A (1s-3d peak), B (first inflection point), C (second inflection point) and D (principal maximum). All four points show a decrease in energy on discharge, although points B and C are somewhat sensitive to the details of the edge shape and thus somewhat more variable. The energy of point A as a function of discharge/charge capacity is shown in Fig. 3d, and the energies for all 4 points are tabulated in Table S1a and b. Using either A or D, the decrease in edge energy during discharge is 1.8–2.1 eV, (an average of $\sim 2 \text{ eV}$) while during charge the increase in edge energy is 1.6–1.8 eV (an average of 1.7 eV) [see Table S1a and b for details]. The slightly smaller shift of the edge energy during the charge

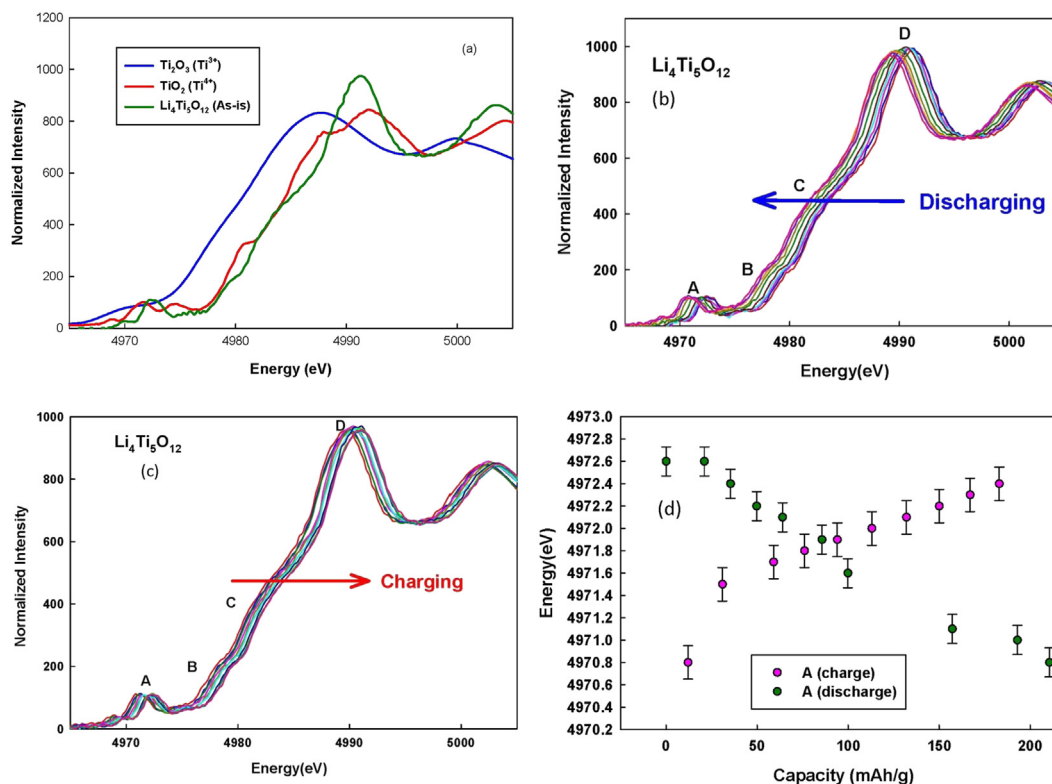


Fig. 3. (a) Ti–K edge XANES of $\text{Li}_4\text{Ti}_5\text{O}_{12}$ Compared to the model compounds Ti_2O_3 and TiO_2 ; (b) *In-situ* Ti–K edge XANES during discharge at capacities shown in Table S1a (Supplementary); (c) *In-situ* Ti–K edge XANES during charge at capacities shown in Table S1b (Supplementary); (d) position of Feature A with respect to capacity during cycling. The galvanostatic cycling of the *in-situ* studies was performed at a current density of 175 mA g^{-1} , between 2.5 V and 1.0 V. Error bars are the estimated standard deviation in replicate measurements.

compared to discharge is due to the slight loss of capacity during the charging cycle.

The data in Fig. 3 provide direct evidence that electrons are added to and removed from a band of primarily Ti character during cycling. For the model compounds, the change in energy on going from Ti(III) to Ti(IV) is $\sim 3.8 \text{ eV}$, with the peak shifting from 4987.5 to 4991.3 eV as shown in Fig. 3a. This empirical correlation of $\sim 3.8 \text{ eV}$ per unit change in oxidation state allows us to estimate the change in average oxidation state from the change energy, with an estimated uncertainty of $\sim 10\%$ based on the variability in edge shift, depending on which point is measured. The *in situ* XANES data thus suggest that during complete discharge the Ti is reduced to an average oxidation state of $\sim \text{Ti}^{3.5+}$, while during charging the Ti is re-oxidized back to an average oxidation state of $\sim \text{Ti}^{3.9+}$. It is noteworthy that at the start of the charge cycle (capacity of 11.7 mAh g^{-1} , Table S1b) the Ti has already returned $\sim 40\%$ of the way to the starting energy, suggesting that there was some relaxation in the discharged battery. If the XANES estimate of average oxidation state is correct, this would imply a stoichiometry of $\text{Li}_{6.5}\text{Ti}_5\text{O}_{12}$ in the fully discharged material.

The XANES region for a relatively ordered material such as $\text{Li}_4\text{Ti}_5\text{O}_{12}$ depends on the details of the atomic arrangements within 5–10 Å of the Ti. While this means that changes in XANES structure are a sensitive reporter of changes in local structure, it also effectively precludes quantitative analyses of XANES structure, since there are far more adjustable parameters than there are observable spectral features. The lack of any significant change in XANES shape during charge or discharge is thus direct evidence that there are no significant structural perturbations to the local Ti environment. The weak peak at $\sim 4972 \text{ eV}$ (labeled A in Fig. 3b) is identified as a 1s–3d transition, and can be used to characterize the electronic structure

of the Ti. While there should, in principle, be two or more resolved 1s–3d transitions due to crystal-field splitting, we observe only a single peak. Neither the shape (i.e., full-width at half-maximum intensity) nor the intensity of the 1s–3d transition changes during cycling, although (as noted above) the energy of the peak shifts with the rest of the edge. From model compound studies, it is known that the 1s–3d peak is most intense for 4-coordinate Ti and least intense for 6-coordinate Ti [35,36]. The low intensity of the 1s–3d transition in mesoporous $\text{Li}_4\text{Ti}_5\text{O}_{12}$ is consistent with an octahedral Ti environment as expected for $\text{Li}_4\text{Ti}_5\text{O}_{12}$, and the lack of change in intensity indicates that this geometry is retained during discharge.

The EXAFS data provides information about the local structure of the Ti ions in $\text{Li}_4\text{Ti}_5\text{O}_{12}$. The Fourier transforms (FT, Fig. 4) show that in all cases the EXAFS is dominated by Ti–O nearest-neighbor scattering and Ti–Ti next-nearest-neighbor scattering. Although Li must also be present in the environment around the Ti, the Li atoms are too light to make a detectable contribution to the EXAFS. The lack of any significant change in the FTs confirms the conclusion from the XANES that the local Ti environment does not change significantly during discharge or charge cycling. The data for each state of charge were fit using a Ti–O shell and a Ti–Ti shell with the bond length (R) and Debye–Waller factor (σ^2) for each shell treated as variable parameters (complete fit data are given in Table S2, Supplementary material). For these fits, the Ti–O coordination number was fixed at 6. The Ti–Ti coordination number should ideally be 5, given that the octahedral site (16d) in $\text{Li}_4\text{Ti}_5\text{O}_{12}$ is occupied with a 1:5 ratio of Li:Ti and only the latter is expected to give a detectable EXAFS signal. A close observation of the FTs during the discharge and charge (Fig. 4) shows that for the Ti–O peaks during discharge, decreases from start to 49.7 mAh g^{-1} and the

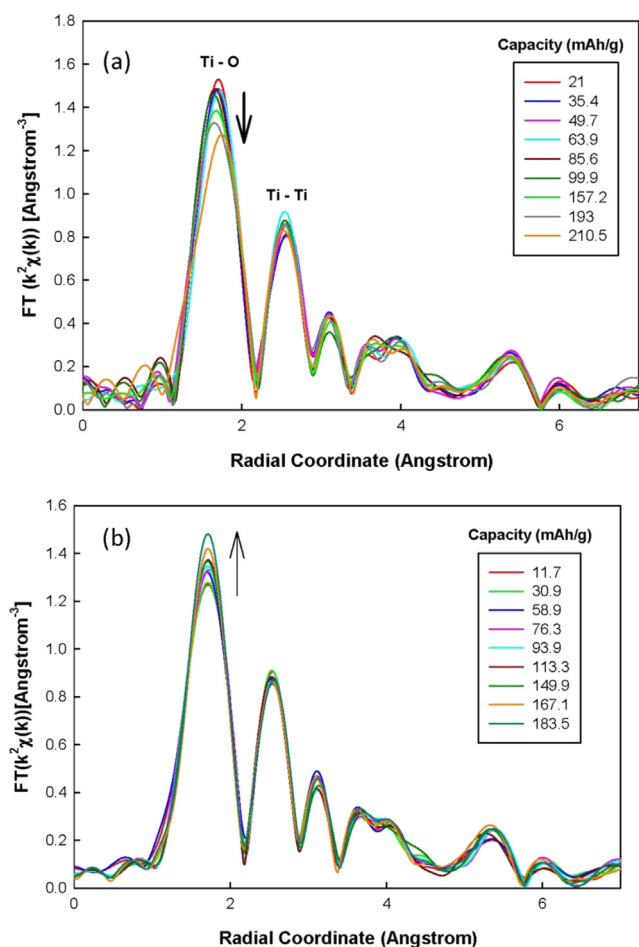


Fig. 4. Magnitude of the k^2 -weighted Fourier transform of $\text{Li}_4\text{Ti}_5\text{O}_{12}$ at the Ti K edge at selected capacity values during the discharge cycle (a) and the charge cycle (b).

almost remains the same till 85.6 mAh g^{-1} and then starts to decrease again till 210.5 mAh g^{-1} . For the charge, the Ti–O peak slowly increases in intensity throughout the cycle.

The accuracy of EXAFS bond length determination is typically taken as $\sim 0.02 \text{ \AA}$ and the observed Ti–O distance for $\text{Li}_4\text{Ti}_5\text{O}_{12}$ is in agreement with the Ti–O distance predicted from neutron diffraction data for $\text{Li}_4\text{Ti}_5\text{O}_{12}$ (1.99 \AA) [37]. However, the precision of EXAFS bond-length determination is much better than its accuracy; we find empirically that the root-mean-square deviation in duplicate bond length measurements is 0.0019 \AA (see Supplementary material). As a consequence, even though the accuracy is only $\sim 0.02 \text{ \AA}$, we are nevertheless able to detect small change in Ti–O distance as a function of charge state. As expected, the average Ti–O distance increases as the Ti is reduced and decreases again as the Ti is reoxidized (see Fig. 5). The total decrease on charging is smaller ($\sim 0.007 \text{ \AA}$); however, careful examination of the data (Fig. 5) suggest that this is not due to irreversibility but rather to partial recovery of the Ti oxidation state prior to initiation of the charge cycle since the starting distance for the charge cycle is already reduced from the endpoint of the discharge cycle. This is similar, to the behavior seen for the XANES.

The observed increase in the Ti–O distance (0.012 \AA) is significantly smaller than the increase that might have been expected from the difference in the ionic radii of Ti^{4+} (0.75 \AA) and Ti^{3+} (0.81 \AA). The neutron diffraction data for chemically lithiated for $\text{Li}_4\text{Ti}_5\text{O}_{12}$ was interpreted as showing a movement of oxide anions

towards octahedral site 16c as lithiation proceeds, presumably to better shield the added lithium cations. The shift in oxide position leads to a predicted increase in Ti–O distance of ~ 0.0213 for $\text{Li}_{6.5}\text{Ti}_5\text{O}_{12}$. Although the actual change is somewhat smaller, our data thus confirm *in-situ* the prediction that was made from chemically lithiated materials.

As noted previously, an unusual feature of $\text{Li}_4\text{Ti}_5\text{O}_{12}$ is the fact that even when discharged down to 0.05 V vs. Li/Li^+ , (i.e., to $\text{Li}_{8.5}\text{Ti}_5\text{O}_{12}$) there is only a small, 0.4%, volume expansion [38]. Although small, the 1% increase in Ti–O distance that we see would by itself seem to imply a larger change in unit cell volume on discharge. The explanation for this anomalous result was noted above – the expansion in Ti–O distance results from movement of the oxide anions to better screen the added lithium, with no predicted change in Ti position. Consistent with this, we see no change in the EXAFS-detected Ti–Ti distance, in agreement with the zero-strain behavior seen for micron to nano sized chemically lithiated materials [37]. It is this rigidity that allows the material to undergo repeated redox cycling without degradation. These observations imply a decrease in Li–O and Ti–Li distances. These are not detectable in the present experiment, but have been seen very recently using *in situ* neutron diffraction (which gave similar inferred changes in Ti oxidation state during cycling) [39].

4. Conclusions

Mesoporous $\text{Li}_4\text{Ti}_5\text{O}_{12}$ microspheres, assembled from nano-sheets, were synthesized successfully and investigated as the anode materials in lithium-ion batteries. The material prepared by hydrothermal reaction showed a large surface area, exhibiting excellent cyclability and high capacity retention. It exhibits high capacity retention of 140 mAh g^{-1} even after 4000 cycles and can even be cycled at high current density of 10^4 mA g^{-1} showing its high promise to applications as an anode material in high rate Li-ion batteries. *In-situ* X-ray absorption spectroscopy confirmed that electrons are added (on discharge) and removed (on charge) from a band of primarily Ti character; the apparent average oxidation state of the fully discharged material is $\sim \text{Ti}^{3.5+}$. The first cycle of charge and discharge EXAFS results showed small changes Ti–O distance but no change in Ti–Ti distance reflecting the fact

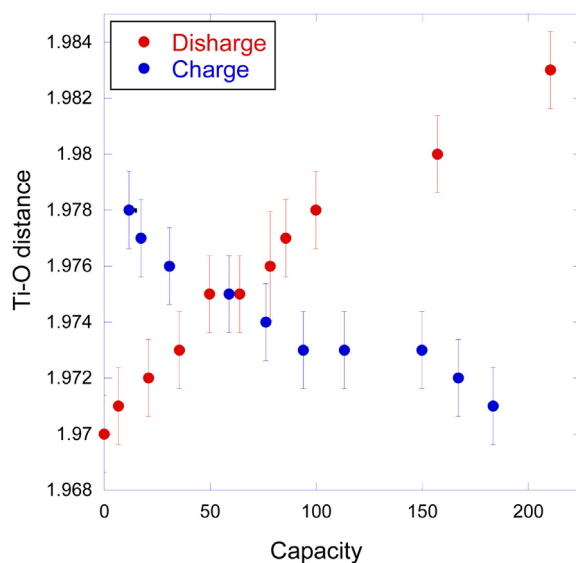


Fig. 5. Fitted Ti–O bond length for $\text{Li}_4\text{Ti}_5\text{O}_{12}$ during discharge and charge cycle. Error bars are estimated standard error of fitted distance (see Supplementary material).

that in this material, lithiation has the effect of pulling the oxide anions closer together, allowing the Ti–O distance to expand, as required on Ti reduction, with negligible change in the lattice parameter.

Acknowledgment

We are grateful for financial support from a University of Michigan, USA–Shanghai Jiao Tong University, China collaborative research project. Li Yang, acknowledge the National Natural Science Foundation of China (Grants No. 21103108 and 21173148). We acknowledge the DND-CAT (5-BM-D) beamline at APS. DND-CAT is supported by the E.I. DuPont de Nemours and Co., The Dow Chemical Company, the U.S. National Science Foundation through Grant DMR-9304725 and the State of Illinois through the Department of Commerce and the Board of Higher Education Grant IBHEHECANWU96.

Appendix A. Supplementary data

Supplementary data related to this article can be found at <http://dx.doi.org/10.1016/j.jpowsour.2014.06.018>.

References

- [1] M.S. Whittingham, *Science* 192 (1976) 1126.
- [2] L. Cheng, J. Yan, G.N. Zhu, J.Y. Luo, C.X. Wang, Y.Y. Xia, *J. Mater. Chem.* 20 (2010) 595.
- [3] A.K. Padhi, K.S. Nanjundaswamy, J.B. Goodenough, *J. Electrochem. Soc.* 144 (1997) 1188.
- [4] B. Scrosati, *Nature* 373 (1995) 557.
- [5] C. Jiang, M. Ichihara, I. Honma, H.S. Zhou, *Electrochim. Acta* 52 (2007) 6470.
- [6] M. Wagemaker, A. Van Der Ven, D. Morgan, G. Ceder, F.M. Mulder, G.J. Kearley, *Chem. Phys.* 317 (2005) 130.
- [7] M. Wagemaker, D.R. Simon, E.M. Kelder, J. Schoonman, C. Ringpfel, U. Haake, D. Lutzenkirchen-Hecht, R. Frahm, F.M. Mulder, *Adv. Mater.* 18 (2006) 3169.
- [8] V. Borgel, G. Gershtinsky, T. Hu, M.G. Theivanayagam, D. Aurbach, *J. Electrochem. Soc.* 160 (2013) A650.
- [9] G.N. Zhu, Y.G. Wang, Y.Y. Xia, *Energy Environ. Sci.* 5 (2012) 6652.
- [10] J.Z. Chen, L. Yang, S.H. Fang, Y.F. Tang, *Electrochim. Acta* 55 (2010) 6596.
- [11] H.B. Wang, Q.M. Pan, Y.X. Cheng, J.W. Zhao, G.P. Yin, *Electrochim. Acta* 54 (2009) 2851.
- [12] H. Qiao, Y.W. Wang, L.F. Xiao, L.Z. Zhang, *Electrochem. Commun.* 10 (2008) 1280.
- [13] B.X. Li, G.X. Rong, Y. Xie, L.F. Huang, C.Q. Feng, *Inorg. Chem.* 45 (2006) 6404.
- [14] Y.G. Guo, J.S. Hu, L.J. Wan, *Adv. Mater.* 20 (2008) 4384.
- [15] A.M. Cao, J.S. Hu, H.P. Liang, L.J. Wan, *Angew. Chem. Int. Ed.* 44 (2005) 4391.
- [16] Y.F. Tang, L. Yang, Z. Qiu, J.S. Huang, *Electrochem. Commun.* 10 (2008) 1513.
- [17] Z.G. Yang, D. Choi, S. Kerisit, K.M. Rosso, D.H. Wang, J. Zhang, G. Graff, J. Liu, *J. Power Sources* 192 (2009) 588.
- [18] S.H. Yu, A. Pucci, T. Hertrich, M.G. Willinger, S.H. Baek, Y.E. Sung, N. Pinna, *J. Mater. Chem.* 21 (2011) 806.
- [19] J. Lu, C.Y. Nan, Q. Peng, Y.D. Li, *J. Power Sources* 202 (2012) 246.
- [20] A. Deb, U. Bergmann, E.J. Cairns, S.P. Cramer, *J. Synchrotron Radiat.* 11 (2004) 497.
- [21] C. Rumble, T.E. Conry, M. Doeff, E.J. Cairns, J.E. Penner-Hahn, A. Deb, *J. Electrochem. Soc.* 157 (2010) A1317.
- [22] T.C. Weng, G.S. Waldo, J.E. Penner-Hahn, *J. Synchrotron Radiat.* 12 (2005) 506.
- [23] M. Newville, *J. Synchrotron Radiat.* 8 (2001) 322.
- [24] J.A. Victoreen, *J. Appl. Phys.* 19 (1948) 855.
- [25] J.J. Rehr, J.J. Kas, F.D. Vila, M.P. Prange, K. Jorissen, *Phys. Chem. Chem. Phys.* 12 (2010) 5503.
- [26] S.C. Lee, S.M. Lee, J.W. Lee, J.B. Lee, S.M. Lee, S.S. Han, H.C. Lee, H.J. Kim, *J. Phys. Chem. C* 113 (2009) 18420.
- [27] L.F. Shen, C.Z. Yuan, H.J. Luo, X.G. Zhang, K. Xu, Y.Y. Xia, *J. Mater. Chem.* 20 (2010) 6998.
- [28] C.X. Qiu, Z.Z. Yuan, L. Liu, N. Ye, J.C. Liu, *J. Solid State Electrochem.* 17 (2013) 841.
- [29] J. Kim, J. Cho, *Electrochem. Solid State* 10 (2007) A81.
- [30] Z.M. Liu, N.Q. Zhang, K.N. Sun, *J. Mater. Chem.* 22 (2012) 11688.
- [31] S.L. Chou, J.Z. Wang, H.K. Liu, S.X. Dou, *J. Phys. Chem. C* 115 (2011) 16220.
- [32] L. Gao, R. Liu, H. Hu, G. Li, Y. Yu, *Nanotechnology* 25 (2014) 175402.
- [33] J.M. Feckl, K. Fominykh, M. Dobliger, D. Fattakhova-Rohlfing, T. Bein, *Angew. Chem. Int. Ed.* 51 (2012) 7459.
- [34] K.S. Jun Liu, Peter A. van Aken, Joachim Maier, Yan Yu, *Nano. Lett. ASAP* (2014), <http://dx.doi.org/10.1021/nl5004174>.
- [35] F. Farges, G.E. Brown, J.J. Rehr, *Geochim. Cosmochim. Acta* 60 (1996) 3023.
- [36] F. Farges, G.E. Brown, J.J. Rehr, *Phys. Rev. B* 56 (1997) 1809.
- [37] W.J.H. Borghols, M. Wagemaker, U. Lafont, E.M. Kelder, F.M. Mulder, *J. Am. Chem. Soc.* 131 (2009) 17786.
- [38] Z.Y. Zhong, C.Y. Ouyang, S.Q. Shi, M.S. Lei, *ChemPhysChem* 9 (2008) 2104.
- [39] V.K.P.W.K. Pang, N. Sharma, J.-J. Shiu, S.-H. Wu, *Chem. Mater.* 26 (2014) 2318.